



In-vitro and In-vivo Characterization of Nanoparticles for the Treatment of Pancreatic Cancer

Anurima Singh¹, Kavita Patle*², Pankaj Bhardwaj³, Samrin Saddam Husain⁴, Trilok Nath Patel⁵, Lilima Baghel⁶, Kamini Verma⁷, Niharika Dewangan⁷

¹Rungta Institute of Pharmaceutical Education and Research, Kohka – 490024, Bhilai, Chhattisgarh, India

²Rungta College of Pharmaceutical Sciences and Research, Kohka – 490024, Bhilai, Chhattisgarh, India

³Shri Balaji College of Pharmaceutical Sciences, Sakti – 495689, Chhattisgarh, India

⁴DBM College of Pharmacy, Devraha Pithampur – 495671, Chhattisgarh, India

⁵R N Dubey College of Pharmacy, Khorsi – 495556, Janjgir-Champa, Chhattisgarh, India

⁶Rungta College of Pharmaceutical Science and Research, Managed by Krishna Vikash Institute, Near Nandanvan – 492099, Raipur, Chhattisgarh, India

⁷Department of Lifescience, Shri Shankaracharya Professional University, Junwani – 490020, Bhilai, Chhattisgarh, India
Corresponding author email - kavita.kp.684@gmail.com

(Received: 16 September 2024

Revised: 11 October 2024

Accepted: 04 November 2024)

KEYWORDS

Pancreatic cancer;
VISTA antibody;
In-vitro cellular targeting;
In-vivo study;
Nanoparticles

ABSTRACT:

Breaking the poor permeability of immune checkpoint inhibitors (ICIs) caused by the stromal barrier and reversing the immunosuppressive microenvironment are significant challenges in pancreatic cancer immunotherapy. In this study, we synthesized core-shell Fe₃O₄TiO₂ nanoparticles to act as carriers for loading VISTA monoclonal antibodies to form Fe₃O₄TiO₂VISTA_mAb. The nanoparticles are designed to target the overexpressed ICIs VISTA in pancreatic cancer, aiming to improve magnetic resonance imaging-guided sonodynamic therapy (SDT)-facilitated immunotherapy. Laser confocal microscopy and flow cytometry results demonstrate that FTV nanoparticles are specifically recognized and phagocytosed by Panc-2 cells. In vivo experiments reveal that ultrasound-triggered TiO₂ SDT can induce tumor immunogenic cell death (ICD) and recruit T-cell infiltration within the tumor microenvironment by releasing damage-associated molecular patterns (DAMPs). Furthermore, ultrasound loosens the dense fibrous stroma surrounding the pancreatic tumor and increases vascular density, facilitating immune therapeutic efficiency. In summary, our study demonstrates that FTV nanoparticles hold great promise for synergistic SDT and immunotherapy in pancreatic cancer.

1. Introduction

Pancreatic ductal adenocarcinoma (PDCA) is a malignant tumor known for its subtle onset and extremely unfavorable treatment outcomes and prognosis [1]. With the emergence of immunotherapy, immune checkpoint therapy presents distinctive advantages, offering novel avenues for treating PDACs. It has been confirmed that PDACs express a range of immune checkpoints involved in immune escape, including PD-1, PD-L1, CTLA-4, and VISTA. Notably,

VISTA exhibits significantly higher expression levels in cancer cells and stromal cells in PDACs than PD-1/PD-L1, and it is also highly expressed in the tumor microenvironment and metastatic lymph nodes [2]. In recent years, the pre-clinical activity of CA-170, a novel dual inhibitor of VISTA and PD-L1, has been investigated [3]. Administration of CA-170 in patients with advanced solid cancers has shown a clinical benefit rate. Specifically, in lung cancer patients, this medication has shown significant improvement in



progression-free survival [4]. Given to the immunosuppressive properties of VISTA, treatment with VISTA antibodies not only significantly prolonged the survival of pancreatic cancer-bearing mice but also clinical trials revealed a negative correlation between VISTA expression levels and survival in patients with primary PDACs [5]. Hence, VISTA emerges as a highly promising target for immune checkpoint therapy in PDACs. Nevertheless, the substantial presence of dense fibrous stroma encircling PDACs impedes the effective infiltration of therapeutic VISTA antibodies. Furthermore, this fibrous stroma is pivotal for facilitating immune escape within PDACs [6]. In pancreatic cancer, dendritic cells often exhibit an immature phenotype and sparsely distribute in the tumor microenvironment, which hinders the process of antigen recognition and subsequently diminishes the activation of T cells [7]. These factors could potentially restrict the application of VISTA in the clinical treatment of pancreatic cancer. Hence, a formidable challenge in treating pancreatic cancer lies in surmounting the formidable barrier posed by the dense fibrous stroma, which could enhance VISTA antibody accumulation and promote T-cells infiltrating the microenvironment [8]. Therefore, choosing the practical approach to break the stromal barrier, increase the immune checkpoint inhibitors concentration, and reverse the immunosuppressive is the current hot spot in immune therapy of PDACs. Mechanical forces such as local thermal ablation and focused ultrasound can loosen the fibrous stroma barrier of PDACs, thereby enhancing the intra-tumoral penetration of drugs [9]. Our recent research findings indicate that photothermal therapy can potentially loosen the stromal barrier and improve drug penetration within pancreatic tumors [10]. Multiple preclinical studies have also showcased

therapeutic benefits when combining phototherapy with ICIs [11]. However, due to limitations in tissue penetration depth, near-infrared light-triggered phototherapy remains a challenge in treating deep-seated tumors like PDACs [12]. In contrast, ultrasound can penetrate soft tissues up to a depth of 10 cm, making ultrasound-based sonodynamic therapy (SDT) a more promising choice for treating PDACs. The potential of SDT for treating pancreatic cancer has been substantiated through a series of preclinical models, and the combination of SDT with ICIs can enhance the therapeutic outcomes [13–15]. When it comes to SDT-based immune checkpoint therapy, one of the paramount concerns lies in the meticulous design of optimal sonosensitizers for the delivery of ICIs. As a critical catalytic material, titanium dioxide (TiO₂) nanoparticles possess advantages such as excellent biocompatibility and stable catalytic performance, making them widely utilized as sonosensitizers in cancer SDT [16–18]. Huang and colleagues recently utilized hollow TiO₂ nanoparticles (NPs) in SDT of subcutaneous xenograft models of human pancreatic cancer. This approach effectively disrupted the fibrous stroma barrier, enhanced tumoral vascular density, and restrained tumor growth. Furthermore, SDT can trigger immunogenic cell death (ICD), amplifying the potential of immune checkpoint therapy by causing necrotic apoptosis in tumor cells and releasing tumor antigens. This process fosters antigen presentation, stimulates the maturation of dendritic cells (DCs), and augments the activation and infiltration of T cells [19–20]. Lin's group demonstrated that combining ultrasound-triggered TiO₂ NPs with PD-L1 antibodies can effectively stimulate immunotherapy in both primary cervical tumor models and their metastatic counterparts [21]. Therefore, considering the challenges associated



with immune therapy and the high expression of VISTA in pancreatic cancer, combining TiO₂-based SDT with VISTA antibody treatment holds the promise to break through the barrier of immunotherapy for pancreatic cancer. In this study, we prepared core-shell nanoparticles composed of Fe₃O₄TiO₂ with a layered shell structure to serve as carriers to load VISTA monoclonal antibodies, forming Fe₃O₄TiO₂VISTAmAb (FTV) NPs [22]. The layered shell structure of Fe₃O₄TiO₂ has multiple catalytic active sites and provides ample space for loading VISTAmAb. The Fe₃O₄ core in the nanoplateforms confers magnetic resonance imaging (MRI) capability, allowing for the visualization of the therapeutic process. As illustrated in Scheme 1, ultrasound treatment loosens the fibrous stroma and enhances the accumulation of FTV within the pancreatic tumor. Subsequently, ultrasound-triggered SDT of TiO₂ induces apoptosis in cancer cells, leading to the release of calreticulin (CRT) and high mobility group box 1 (HMGB-1), which in turn recruits and activates T cells. Simultaneously, VISTAmAb blocks the VISTA immune checkpoints and initiates T cell immunotherapy [23].

2. Material and Methods

Synthesis and characterization of the nanoparticles

A schematic illustration of the brief Fe₃O₄TiO₂VISTAmAb (FTV) formation was presented in Scheme 1. The magnetic Fe₃O₄ NPs were prepared by solvothermal method, and Fe₃O₄SiO₂ NPs were formed by surface modification of Fe₃O₄ with TEOS. Then, Fe₃O₄SiO₂TiO₂ NPs were synthesized by coating TBOT on the surface of Fe₃O₄SiO₂. Finally, the SiO₂ layer was etched by NaOH, and Fe₃O₄TiO₂ (FT) NPs were obtained. A larger cavity structure remained after etching, which is believed to enhance the ultrasonic catalytic performance of titanium

nanomaterials. Transmission electron microscopy was carried out to determine the size and microstructure of as-prepared nanoparticles. As shown in Figs. S1A–S1C, the diameter of core Fe₃O₄, Fe₃O₄SiO₂, and Fe₃O₄SiO₂TiO₂ NPs are 50 nm, 95 nm, and 130 nm, respectively. Fig. 1A and B shows that the FT NPs are relatively homogeneous, with an average diameter of about 120 nm. Energy dispersive X-ray (EDX) elemental mappings reveal a uniform Fe, Si, and O elements distribution within FT NPs (Fig. 1C). The crystal structure of FT NPs was analyzed by powder X-ray diffraction (XRD) (Fig. S2). VISTAmAb, an immune checkpoint inhibitor, was electrostatically adsorbed onto Fe₃O₄TiO₂ to construct Fe₃O₄TiO₂VISTAmAb (FTV) NPs. As shown in Fig. 1D, following the adsorption of VISTAmAb, the FTV NPs exhibit a newly emerged peak at 1735 cm⁻¹, attributed to the stretching vibration peak of C–O [24–25]. The dynamic light scattering (DLS) results show the hydrodynamic size and zeta potential of FTV NPs are around 215 nm and -28.9 mV, respectively (Figs. 1E and 2F).

3. Results and Discussion

The SDT and MRI performance of FTV

One of the primary mechanisms of SDT is the stimulation of sonosensitizers by ultrasound to generate reactive oxygen species (ROS), leading to the apoptosis of cancer cells. Hence, the yield of ROS is closely related to the effectiveness of SDT. Previous reports have demonstrated that titanium nanomaterials with large cavity structures and high specific surface areas possess more catalytic sites and exhibit high catalytic activity [26–28]. To verify the ultrasonic catalytic activity of the prepared FTV, we used commercial titanium dioxide nanoparticles and H₂O as a control group for comparison. The compound 1, 3-diphe-



nylisoben-zofuran was used to detect the ROS production of ultrasound-irradiated FTV. The ROS production causes the oxidation of DPBF, converting it into colorless 1,2-dibenzoylbenzene. A mixture of DPBF and FTV NPs was exposed to ultrasound, and the UV-Vis absorption spectra of DPBF were tested. The DPBF peaks exhibit a decreasing trend as the duration of ultrasound exposure extends, indicating a corresponding rise in the production of ROS [29]. After a series of ultrasound exposure times (1–8 min), the peaks decrease from 94.97 % to 70.06 % (Fig. 2A). In contrast, commercial TiO₂ (P25) shows less variation in peak value for the same ultrasound irradiation time (Fig. 2B and Fig. S3). Therefore, FTV NPs have better ROS production efficiency and SDT performance than P25, which can be attributed to their high specific surface area and numerous catalytic active sites. A 0.5 T MRI scanner was used to evaluate the magnetic resonance properties of the NPs. The longitudinal relaxation rate (r_1) value of FTV NPs is 1.57 Mm⁻¹ s⁻¹ at the same Fe₃O₄ concentration. The transverse relaxation rate (r_2)

value of FTV NPs is 50.28 Mm⁻¹ s⁻¹ (Fig. 2D). The FTV NPs exhibit an r_2/r_1 value of about 32.03, signifying their effectiveness as MRI T₂ contrast agents. As depicted in Fig. 2C, the T₂ dark signal is enhanced with increasing concentrations of FTV NPs [30].

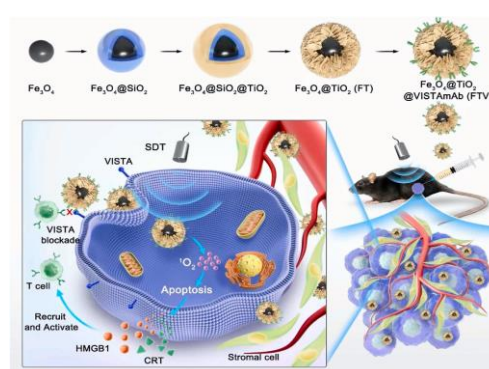


Fig. 1. The preparation process of Fe₃O₄TiO₂VISTAmAb NPs and combining TiO₂-based SDT with VISTA antibody treatment in pancreatic cancer.

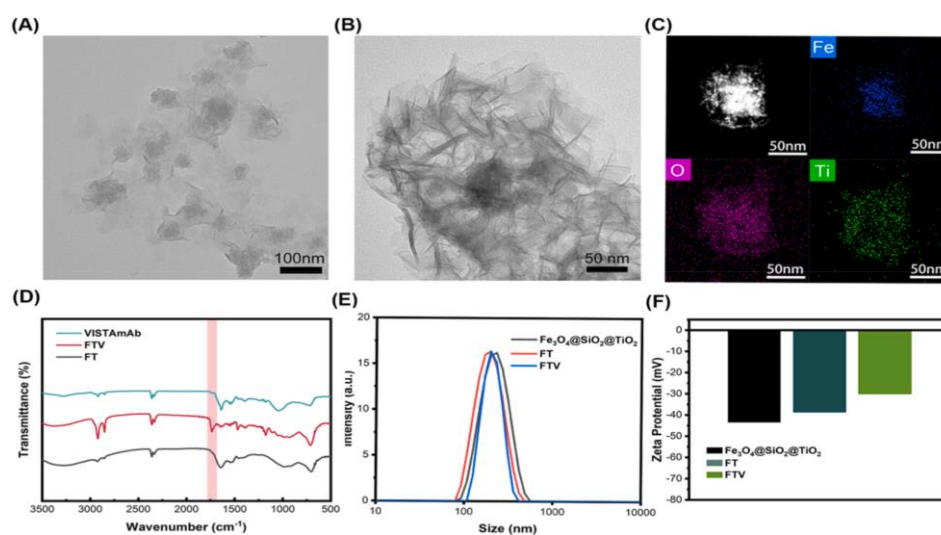


Fig. 2. A) and B) TEM images of FT NPs. C) High-angle annular dark field imaging and EDS elemental mapping of FT. D) Micro-FTIR test of VISTAmAb, FT and FTV. E) Particle size of Fe₃O₄SiO₂TiO₂, FT, and FTV. F) Zeta potential.

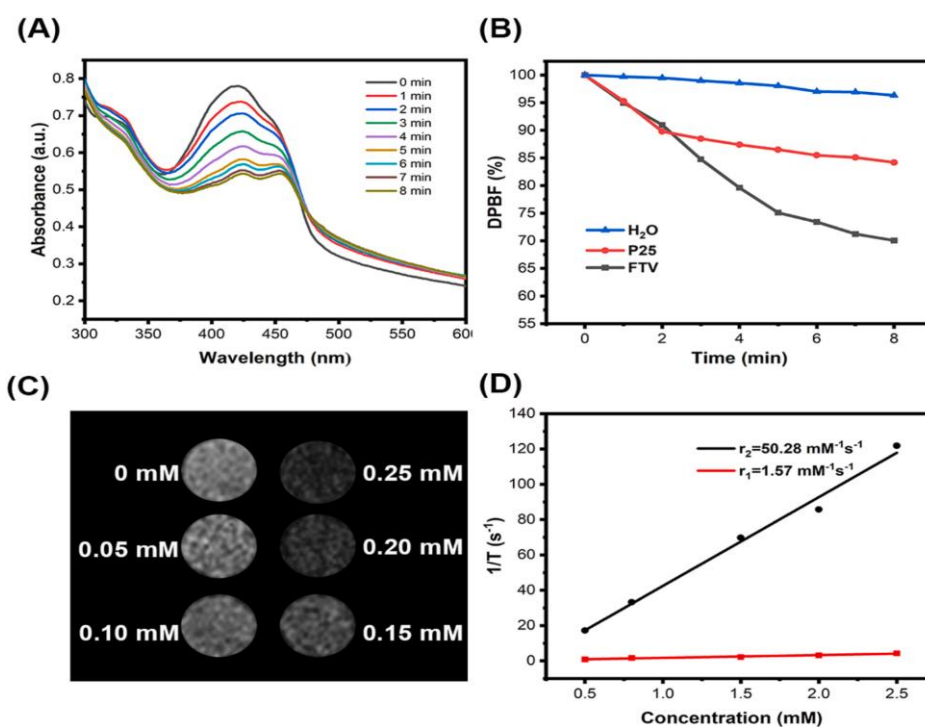


Fig. 3. A) UV-vis absorption curves of DPBF in FTV aqueous solution with ultrasonic irradiation at different times. B) The DPBF relative concentrations of ultrasound irradiated H₂O, P25 and FTV, respectively. C) T₂-weighted MR imaging of FTV at different Fe concentrations. US irradiation (1.0 MHz, 1.5 W cm⁻², 50 % duty cycle) was carried out in applicable groups. D) The relaxation curves of FTV.

In-vitro cellular targeting uptake

As previously mentioned, VISTA is highly expressed in both pancreatic cancer and stromal cells, rendering it an ideal target for nanoparticle-based targeted therapy. Therefore, we selected the cell lines with high VISTA expression using western blot analysis. As illustrated in Fig. S4, pancreatic cancer cells (Panc-1 and Panc-2) exhibit significantly elevated VISTA expression in contrast to normal pancreatic ductal epithelial cells which is consistent with the previous report indicating heightened VISTA expression in pancreatic cancer cells and relatively low expression in normal pancreas. We chose Panc-2 cells for subsequent studies. The cellular uptake of FT NPs and FTV NPs was observed by CLSM. The red fluorescence emitted by rhodamine B-

labeled FT and FTV NPs can trace the intracellular distribution of the NPs. Panc-2 cells were incubated with various concentrations of the materials over different time periods, resulting in an increase in fluorescence intensity that correlated with both time and concentration. Based on these results, the conditions of 50 µg/mL and 4 h were selected for subsequent experiments (Fig. S11). In Fig. 3A and Fig. S5, it can be observed that the red fluorescence in Panc-2 cells incubated with FTV is slightly more intense compared to those set with FT. In addition, the intracellular fluorescence intensity of Panc-2 cells was examined by flow cytometry. In line with the CLSM findings, the fluorescence intensity in the FTV group surpasses that in the FT group, which is also confirmed by



semiquantitative analysis (Fig. 3B and C). Thus, VISTA-modified FT NPs exhibit Panc-2 cell targeting ability, which is expected to enhance the efficacy of SDT.

***In-vitro* SDT**

Prior to evaluating the therapeutic effect at the cellular level, we conducted a CCK-8 assay to assess the cytotoxicity of the NPs. The results in Fig. 4A confirm FT and FTV NPs have no significant toxicity to Panc-2 cells within the experimental concentration range. The cell survival rate reaches approximately 90 % after incubating with the FTV NPs at a concentration of 100 $\mu\text{g mL}^{-1}$ for 24 h. Under US irradiation and

coincubation with nanoparticles ($50 \mu\text{g mL}^{-1}$), cell viability is significantly reduced, decreasing by 56.69 %, as shown in Fig. 4B. A concentration of $50 \mu\text{g mL}^{-1}$ nanoparticles was selected for subsequent experiments due to its notable therapeutic effect without causing apparent cytotoxicity concurrently. In addition, to further prove the SDT cellular effect of FT and FTV NPs, we performed live cell staining by calcein acetoxy methyl ester and dead cell staining by propidium iodide (PI). Fig. 4C reveals that the nanoparticle groups under US irradiation exhibit the most effective anticancer effect, consistent with the results obtained from cell viability in the CCK-8 assay.

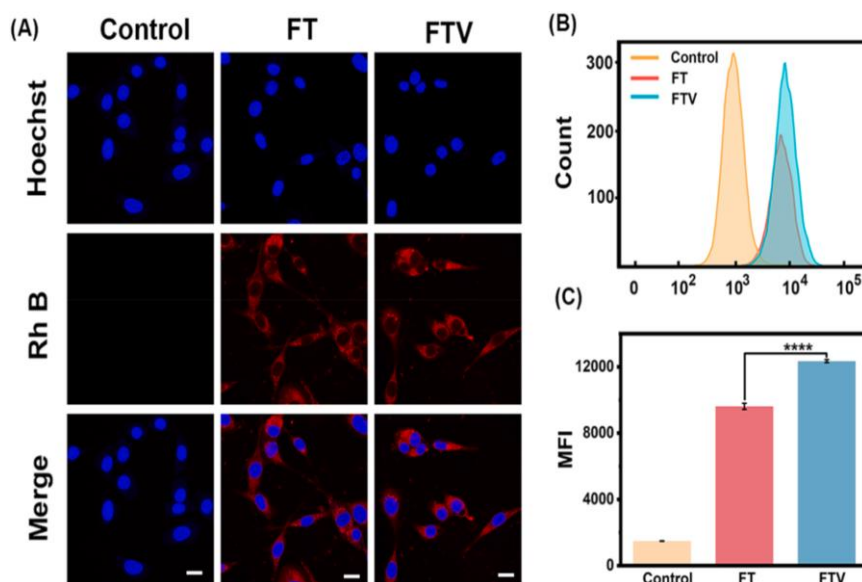


Fig. 4. A) CLSM images of Panc-2 cells incubated with FT or FTV ($50 \mu\text{g mL}^{-1}$) for 4 h. Scale bar: 20 μm . B) The intracellular uptake FT and FTV ($50 \mu\text{g mL}^{-1}$). C) The semiquantitative analysis of (B). All data are presented as means \pm SD from at least three independent experiments. * $p < 0.05$, ** $p < 0.01$, *** $p < 0.001$, **** $p < 0.0001$.

Next, a 2, 7-dichlorofluorescein diacetate probe was used to verify the ROS production at the cellular level, represented by green fluorescence. After co-incubation with nanoparticles and exposure to US irradiation, the

intense green fluorescence observed indicates a substantial increase in intracellular ROS level when compared to other groups (Fig. 4D). This phenomenon demonstrates the intracellular mechanism through



which FT and FTV NPs act as SDT agents. Damage associated molecular patterns (DAMPs) such as calreticulin (CRT) and high mobility group box 1 serve as the biomarker of ICD. CRT is a soluble protein in the lumen of the endoplasmic reticulum (ER) that mediates several functions. During ICD, CRT is exposed on the cell surface, serving as a crucial 'eat me' signal [31-34]. HMGB-1, a highly abundant nuclear non-histone chromatin-binding protein, is released from the nucleus into the extracellular environment of dying cells during ICD [35]. Consequently, CRT expression is upregulated on the cell membrane, while HMGB-1 is downregulated. The expression levels of HMGB-1 and CRT during SDT were investigated using CLSM and FCM. As shown in Fig. 5A and C, the fluorescence intensity of HMGB-1 is notably reduced in FTV + US group, signifying that SDT causes the release of HMGB-1 from the intracellular to the extracellular environment. Furthermore, in the FTV + US group, CRT expression is higher than both FTV and US groups (Fig. 5B and D). These findings indicate that the SDT strategy can enhance the release of DAMPs, thereby potentially elevating ICD [36-38].

***In-vivo* biosafety and anti-tumor effect of the nanoparticles**

To assess the *in-vivo* safety of nanoparticles, we analyzed various biological indicators, including mice' weight, blood, and the condition of their major organs after injecting them with a dose of 15 mg kg⁻¹ of nanoparticles. Blood examinations were conducted on day 14 post injection, and all measured parameters showed no significant differences, confirming the absence of any discernible risk of chronic toxicity (Figs. S6-S8). Hematoxylin and eosin (H&E) staining provides a comprehensive view of major organs after injection with different nanoparticles. The results

presented in Fig. S9 reveal no discernible pathological changes in any organ slices, thus confirming an extremely low level of tissue toxicity. Motivated by the apparent therapeutic effect at the cellular level, we proceeded to assess the *in vivo* therapeutic performance of FTV NPs using the Panc-2 tumor-bearing C57BL/6 mice. All mice were randomly divided into six divisions (n = 5): control, US, FT, FTV, FT + US, and FTV + US group. The mice were intratumorally injected with or without FT or FTV NPs on day 0, and US irradiation was performed after 2 h of injection. Mouse body weights and tumor volumes were recorded every 2 days. During the treatment period of 2 weeks, there was a gradual increase in the mice' body weights, indicating that the treatment had no side effects on the mice (Fig. 6A). As depicted in Fig. 6B, tumors are significantly suppressed in the treated mice of the FTV group, indicating that VISTA-targeted nanoparticles offer therapeutic efficacy in a pancreatic cancer model. In contrast to the control groups, the most significant effect is observed in the FTV + US group, with a tumor weight inhibition index as high as 85.36 % measured on day 14 compared to the control group (Fig. 6B, C and 6D). However, we can see that tumor growth is inhibited in mice after US irradiation without any injection, which may be attributed to the damage inflicted on the tumor cell by the mechanical waves of ultrasound. The tumor growth in the FTV + US group is significantly inhibited after SDT, showing that the nanoparticle-based SDT combined with immunotherapy can achieve better therapeutic effects by generating ROS to induce tumor ICD and trigger an adaptive immune response against the tumor. Moreover, H&E staining results show representative characteristic pyknosis and karyolysis in the FTV + US group, demonstrating a severe disintegration of the cell



nucleus. At the same time, varying degrees of cell damage can be observed in other groups exposed to ultrasound irradiation (Fig. 6E). Additionally, a 3.0 T MR scanning system was employed to evaluate the nanoparticle's *in vivo* MRI performance. FT and FTV NPs were injected into the tumors of different mice (10 mg kg⁻¹), and the MRI pictures were captured after 2 h of injection. The results are shown in Fig. 6F and Fig. S12. The tumor site exhibits strong T2 dark imaging,

accurately visualizing the tumor's size and clear contrast with the surrounding tissues. The MR signal value of PBS, FT and FTV group are 183.87, 42.2 and 44.17, respectively (Fig. S12). Hence, the results confirm that FTV NPs possess MRI T2-weighted imaging capabilities, making them a promising probe for potential tumor treatment visualization.

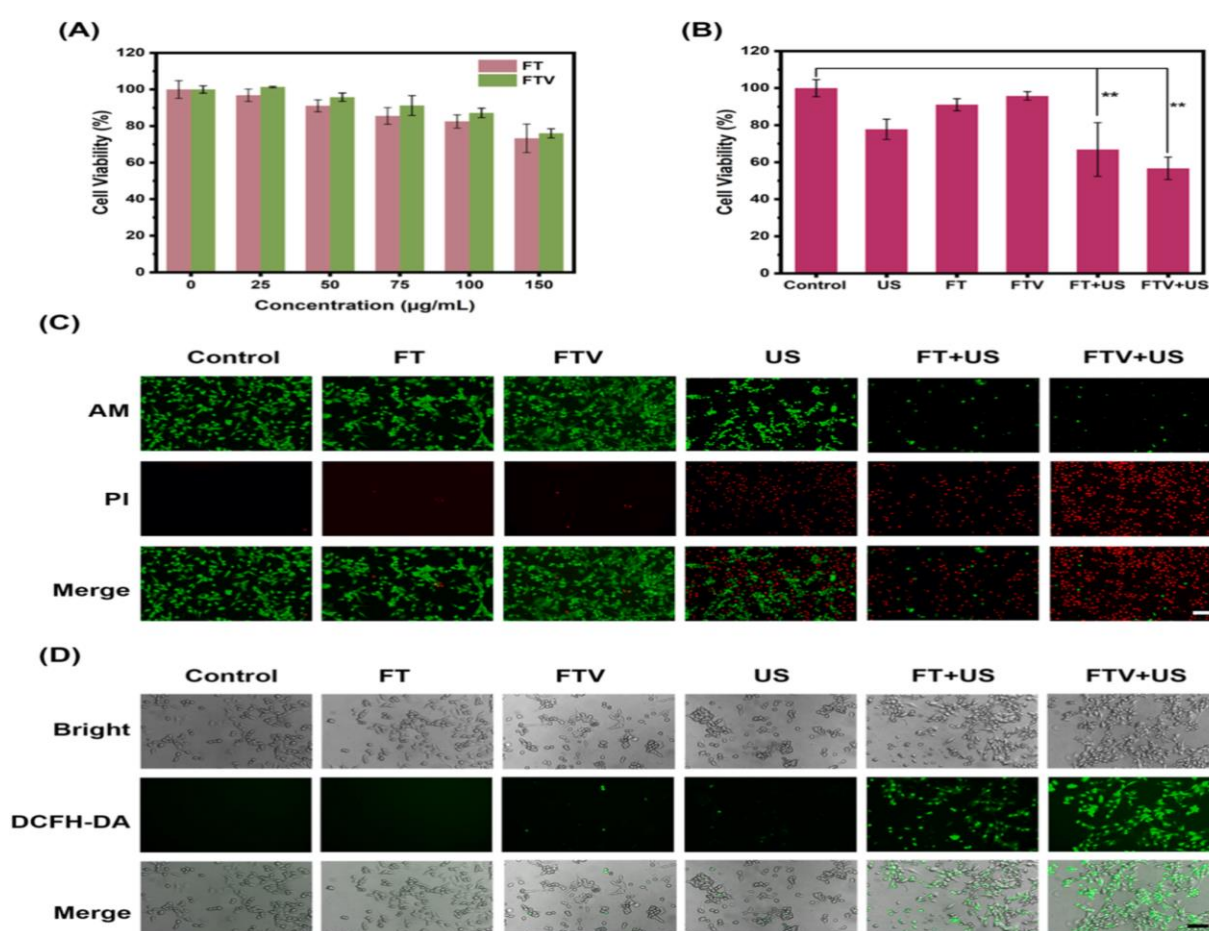


Fig. 5. A) The cell viability of Panc-2 cells co-incubated with FT or FTV. B) Cell survival of Panc-2 cells after different treatments (1.0 MHz, 1 W cm⁻², 1 min, 50 % duty cycle). Scale bar: 50 µm. C) Live/dead cell staining of Panc-2 cells after different treatments (1.0 MHz, 1 W cm⁻², 2 min, 50 % duty cycle). **p* < 0.05, ***p* < 0.01, ****p* < 0.001. D) Detection of ROS production in Panc-2 cells by staining with DCFH-DA after different treatments (1.0 MHz, 0.5 W cm⁻², 1 min, 50 % duty cycle). Scale bar: 50 µm.

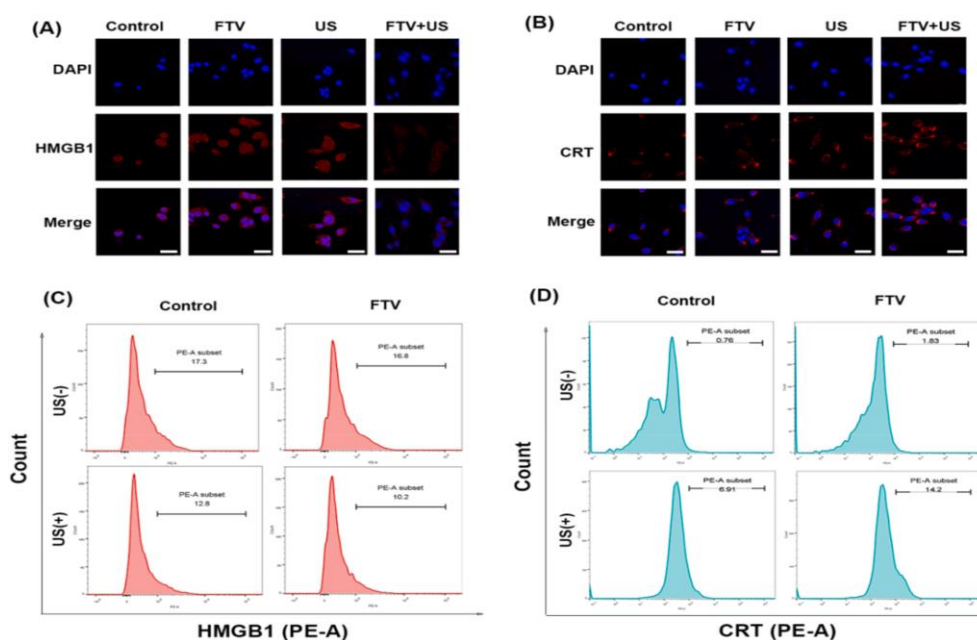


Fig. 6. CLSM images of HMGB1 (A) and CRT (B) expression in Panc-2 cells. Scale bar: 20 μ m. FCM of HMGB1 (C) and CRT (D).

Assessment in tumor microenvironment

Masson staining and CD31 fluorescence staining were conducted on the tumor tissues to characterize the collagen fibers and blood vessels in tumor-bearing mice. The results of Masson staining are shown in Fig. 7A. The blue staining in the results represents collagen fibers, indicating that the pancreatic cancer model exhibits an abundance of collagen fibers, with a substantial amount of stroma surrounding the tumor cells within the interstitium. Ultrasound treatment changes the dense fibrous tissue within pancreatic cancer, disrupting tight junctions between cancer cells. The mechanical force exerted by US may contribute to the damage observed in tumor cells and alter the arrangement of collagen fibers and cells. In Fig. 7B, green fluorescence represents the blood vessels, and there is almost no green fluorescence in the control group, suggesting no capillaries in the tumor. As illustrated in Fig. 7C, the vascular density is enhanced by more than two-fold in the groups exposed to US

compared to the control group. This phenomenon suggests an augmented angiogenesis within the tumor tissue and an elevated density of central blood vessels within the tumor under US influence. These changes can facilitate the penetration of nanoparticles into the tumor's interior and enhance their accumulation. VISTAmAb can stimulate the initial T lymphocytes to further differentiate into cytotoxic T lymphocytes with anti-tumor activity. Therefore, CD4⁺ T cells and CD8⁺ T cells in tumor tissue sections were fluorescently stained using double immunofluorescence to analyze their infiltration in tumor sites. Fig. 7D demonstrates that higher frequencies of CD8⁺ T cells and CD4⁺ T cells are present in tumor sections after injecting FTV nanoparticles compared to other groups. This suggests a significant infiltration of CD8⁺ and CD4⁺ T cells into the tumor microenvironment, indicating a robust anti-tumor immune response. In this study, the immunotherapeutic effect is achieved using VISTAmAb, which antagonizes the VISTA receptor



protein located on the tumor cell membrane. [39] This action reverses the local suppressive immune microenvironment in pancreatic cancer by preventing the binding of immune checkpoint VISTA to ligands on T lymphocytes. Consequently, this approach can activate a T lymphocyte-mediated immune response and prevent immune escape of the tumor cells. To further confirm the immunotherapeutic mechanism, we assessed the expression of immune checkpoints in pancreatic cancer. In Fig. 8A, following treatment with FTV NPs, a noticeable reduction in the yellow-brown staining representing VISTA expression can be

observed. This indicates a decrease in the expression of VISTA at tumor tissue following blockade by antibodies. The expression of VISTA in the tumor tissue is also reduced following treatment with FTV + US (Fig. 8A and B). Furthermore, the expression of PD-1 and PD-L1 was also assessed. Fig. 8C and D and Fig. S11 distinctly reveal the absence of PD-L1 and PD-1 expression in the control group, suggesting that achieving immunotherapeutic effect with anti-PD-L1/PD-1 alone is challenging. However, there is an observed compensatory increase in PD-L1 and PD-1 expression following VISTA-blockade treatment [40].

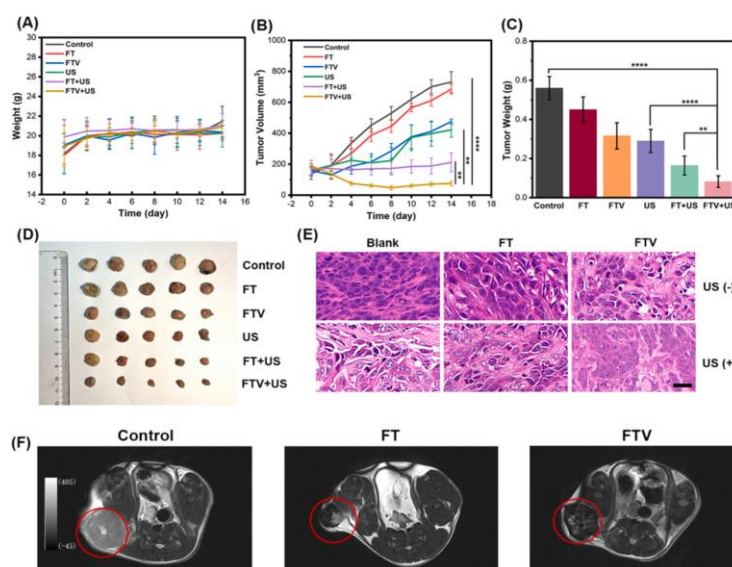


Fig. 7. A) Body weight and B) tumor volume changes of mice treated for 14 days. C) Weight and D) photographs of the tumor on day 14 after treatment. E) H&E staining of tumor tissue after treatment. F) T2-weighted MR imaging before and after the nanoparticle injection. Scale bar: 50 μm . US irradiation (1.0 MHz, 1.5 W cm^{-2} , 50 % duty cycle) was carried out for 3 min in applicable groups. All data are presented as means \pm SD from at least three independent experiments. * $p < 0.05$, ** $p < 0.01$, *** $p < 0.001$, **** $p < 0.0001$.

The increased expression profile occurs after inhibition of other checkpoints, which indicates that the inhibition of one checkpoint will increase the expression of other checkpoints [41-43]. Previous research showed that release of IFN- γ from activated T cells is suppressed by

soluble VISTA, while the application of the dual VISTA/PD-L1 inhibitor restores IFN- γ production [44]. This is suggested that PD-1/PD-L1 blockade therapy also increases the activity of CD8 $^{+}$ T cells and further releasing IFN- γ . It can be postulated that treatment with



anti-VISTA therapy may secondarily cause PD-1/PD-L1 upregulation. This finding may offer new insights into combination therapy involving both anti-PD-

L1/PD-1 and VISTA mAb for enhanced immunotherapy outcomes [45].

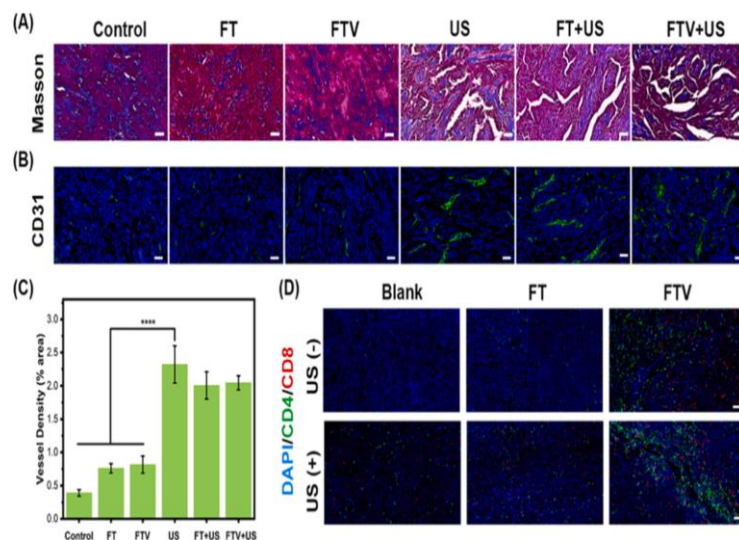


Fig. 8. Tumor tissue staining of different treatment groups (A) Masson and (B) CD31. C) The analysis of CD31 (green color) in (B). D) Immunofluorescence analysis of CD4 and CD8. Scale bar: 50 μ m. All data are presented as means \pm SD from at least three independent experiments. * $p < 0.05$, ** $p < 0.01$, *** $p < 0.001$, **** $p < 0.0001$.

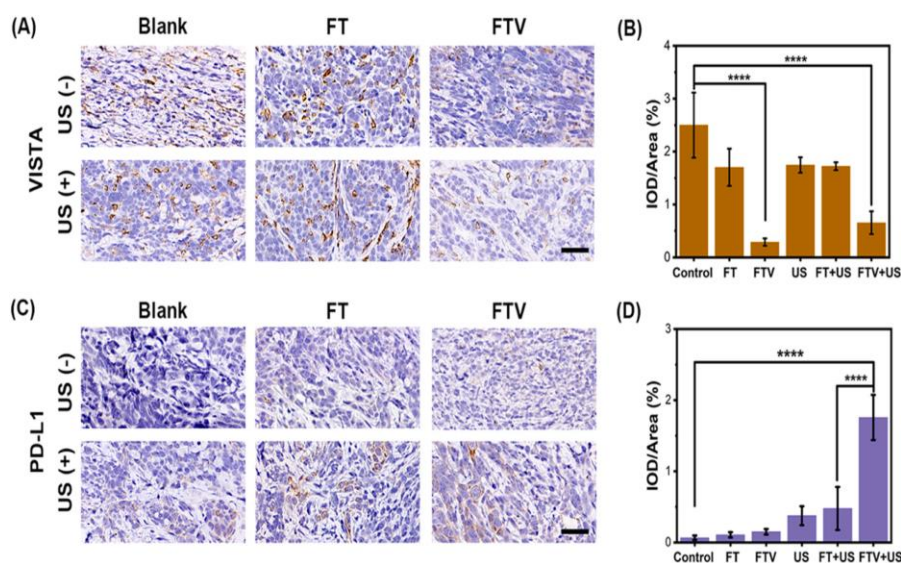


Fig.9. A) Immunohistochemical staining of VISTA. B) The analysis of VISTA expression in (A). C) Immunohistochemical staining of PD-L1. D) The analysis of PD-L1 expression in (C). Scale bar: 50 μ m. All data are presented as means \pm SD from at least three independent experiments. * $p < 0.05$, ** $p < 0.01$, *** $p < 0.001$, **** $p < 0.0001$.



4. Experimental Section

FeCl₃·6H₂O, Tetraethyl orthosilicate, sodium acetate, tetrabutyl titanate, trisodium citrate, Dimethyl sulfoxide, ethanol, ethylene glycol, concentrated ammonia solution (28 wt%), NaOH, HCl, were purchased from Aladdin. Rhodamine B (Rh B) and P25 were purchased from Macklin. 1,3-Diphenylisobenzofuran was purchased from J&K Scientific. FeCl₃·6H₂O (1.62 g), trisodium citrate (1.625 g), and sodium acetate (NaAc, 3.0 g) were dissolved in ethylene glycol (50 mL) with magnetic stirring and heating until the solution turned clarified yellow. The obtained yellow solution was then transferred and sealed into a Teflonlined stainless-steel autoclave (100 mL in capacity). The autoclave was heated at 180 °C for 12 h and then cooled to room temperature. The black magnet products were washed with deionized water and ethanol for 3 times, respectively. The core-shell Fe₃O₄SiO₂ NPs were prepared through a Stober sol gel method. The Fe₃O₄ NPs (45 mg) were added to a three-neck round bottom flask charged with absolute ethanol (80 mL), deionized water (16 mL), and concentrated ammonia solution (2.0 mL, 28 wt%) under ultrasound for 15 min. Then, 0.4 mL of TEOS was added slowly, and hydrolytic reaction for 10 h at room temperature under mechanical stirring. The Fe₃O₄SiO₂ NPs were washed with deionized water and ethanol for 3 times, respectively. The core-shell Fe₃O₄SiO₂TiO₂ NPs were synthesized based on TBOT hydrolytic condensation. The produced Fe₃O₄SiO₂ (150 mg) were redispersed in ethanol (200 mL) and mixed with the concentrated ammonia solution (0.9 mL, 28 wt%) under ultrasound for 15 min. TBOT (1.2 mL) was added dropwise within 5 min, and the reaction was carried out under continuous mechanical stirring (150 rpm) at 45 °C for 24 h. The Fe₃O₄SiO₂TiO₂

nanoparticles were obtained and washed for 3 times. Fe₃O₄TiO₂ NPs were prepared by alkaline hydrothermal corrosionassisted crystallization method. 50 mg of Fe₃O₄SiO₂TiO₂ were sonicated by ultrasonic cell crusher for 5 min, then mixed with NaOH (1 mL, 2.0 M) and H₂O (14 mL) and added into a Teflon-lined stainlesssteel autoclave (20 mL in capacity). The autoclave was heated in an oven at 150 °C for 6 h and then cooled to room temperature. The obtained products were immersed in HCl (10 mL, 0.1 M) for 30 min and then washed with deionized water until the pH value was close to 7. The Fe₃O₄TiO₂ (FT) NPs were dispersed in the deionized water. Fe₃O₄TiO₂VISTAmAb NPs were obtained by mechanical stirring (250 rpm) VISTAmAb (100 µg) and Fe₃O₄TiO₂ (1 mg) in deionized water at 4 °C for 12 h. Finally, Fe₃O₄TiO₂VISTAmAb (FTV) NPs were obtained by centrifugation and washing. Hydrodynamic size and Zeta potential of Fe₃O₄, Fe₃O₄SiO₂, Fe₃O₄SiO₂TiO₂, FT, and FTV were measured by Zeta Sizer Nanoseries instrument (Nano-ZS, Malvern, England) in an aqueous solution at room temperature DPBF was dissolved in DMSO and added to 100 µg mL⁻¹ of FTV solution. After being irradiated by 1 W cm⁻² of ultrasound (1.0 MHz, 50 % duty cycle) for different times, UV-visible absorptions of the solutions were tested in the dark. Meanwhile, commercial P25 nanoparticles were used as control groups, and the results were obtained using the same treatment method. FTV NPs were formulated into solutions with different Fe₃O₄ concentrations (0.05 mM, 0.10 mM, 0.15 mM, 0.20 mM, 0.25 mM) added to tubes. The longitudinal (r₁) and transverse (r₂) relaxation rates of FTV were calculated through the obtained relaxation time values. In addition, T₂-weighted MRI performance was determined for different concentrations of



Fe₃O₄TiO₂VISTAmAb NPs. hTERT-HPNE pancreatic ductal epithelial cells, Panc-1 PDAC cells, Panc-2 PDAC cells, and MIA PaCa-2 PDAC were purchased from the Cell Bank of the Chinese Academy of Sciences. The cells were cultured with DMEM medium containing 10 % FBS, 100 U mL⁻¹ penicillin, 100 U mL⁻¹ streptomycin, and streptomycin in a 37 °C incubator containing 5 % CO₂. The VISTA levels in the hTERT-HPNE pancreatic ductal epithelial cells, Panc-1 PDAC cells, Panc-2 PDAC cells, and MIA PaCa-2 PDAC cells were quantified via western blot analysis. Panc-2 cells (105 per well) were seeded in 35 mm glass-bottom dishes. The cells were co-cultured with Rhodamine B-labeled FT and FTV (50 µg mL⁻¹) for 4 h, respectively, and then were stained by Hoechst. The cellular uptake of FT and FTV was observed by confocal laser scanning microscopy (CLSM). The excitation wavelengths of rhodamine B and Hoechst are 552 nm and 350 nm, and the emission wavelengths are 571 nm and 460 nm, respectively. Panc-2 cells (2 × 10⁵ per well) were inoculated in 96-well plates for 12 h. DMEM medium containing 150, 100, 75, 50, 25, and 0 µg mL⁻¹ of FT or FTV were added and incubated for 24 h. After incubation, the old culture medium was aspirated, and 100 µL of DMEM medium containing 10 µL of CCK-8 solution (5 mg mL⁻¹) was added to each well and incubated for 30 min. The absorbance of each well was recorded at 450 nm using an enzyme marker, respectively. In addition, in vitro SDT of FT and FTV nanoparticles were determined by CCK-8 assay. Panc-2 cells (2 × 10⁵ per well) were inoculated in 96-well plates and incubated with FT or FTV (50 µg mL⁻¹) for 4 h, and then treated with or without ultrasound irradiation according to groups (control, US, FT, FTV, FT + US, FTV + US). The parameters of ultrasound irradiation were 1 W cm⁻² for acoustic power, and 1

min for irradiation time. Then, incubated for another 12 h, the therapeutic effect in vitro was administered by CCK-8 test for cell viability evaluation. Panc-2 cells (2 × 10⁵ per well) were inoculated in 24-well plates for 12 h, incubated with FT or FTV (50 µg mL⁻¹) for 4 h, and then treated with or without ultrasound irradiation according to groups. The parameters of ultrasound irradiation were 1 W cm⁻² for acoustic power, and 2 min for irradiation time. Then, the cells were incubated with the calcein-AM and propidium iodide PI staining. Inverted fluorescence microscopy was used to observe live/dead cell fluorescence imaging. Panc-2 cells (2 × 10⁵ per well) were inoculated in 24-well plates for 12 h. DMEM medium containing 50 µg mL⁻¹ of FT or FTV was added to the plates and incubated for 4 h. Then, the old culture medium was aspirated, and the DCFH-DA probe was added and incubated at 37 °C for 30 min. The cells were treated with ultrasound and incubated for 30 min at 37 °C. Inverted fluorescence microscopy was used to observe intracellular ROS generation. Panc-2 cells (2 × 10⁵ per well) were inoculated in 6-well plates for 12 h or 35 mm glass-bottom dishes. The cells were co-cultured with different NPs for 4 h, followed by ultrasonic irradiation. Then 0.3 % Triton X-100 was permeabilized for 20 min, and 5 % BSA-containing PBS was added to block non-specific binding sites for 30 min. After washing with PBS, the cells were incubated with HMGB1 or CRT antibody (diluted 400 times) at 4 °C overnight. Cells were washed with PBS and then were incubated with the secondary antibody (diluted 400 times) for 1 h. The nuclei were stained with Hoechst for 15 min and imaged with CLSM and flow cytometry (FCM). All the animal experiments were carried out under the guidelines of the Experimental Animal Ethics Committee of Ningbo University. To further evaluate the in vitro biotoxicity of the NPs,



FT/FTV in PBS were injected into 6-week-old Bahl/c female mice (15 mg kg⁻¹), respectively. After 14 days, blood samples were subjected to routine blood and blood biochemical tests. Main organs, such as the heart, liver, spleen, kidney, and lung, were fixed with paraformaldehyde and were evaluated pathologically. For the pancreatic tumor-bearing model, 6-week female C57BL/6 mice were selected, and 3 × 10⁷ Panc-2 cells in 100 μL PBS were injected into the right leg of each mouse. The treatment started when the diameter of tumor reached 5–7 mm. The tumor volumes were calculated as $V = 0.5 \times (\text{length}) \times (\text{width})^2$. Tumor-bearing mice were randomly divided into six groups (n = 5): Control, FT, FTV, US, FT + US and FTV + US. The FT/FTV NPs were intratumorally injected, and the mice were treated with or without ultrasound 1 h after injection. The parameters were 1.5 W cm⁻², 3 min, 1 MHz, and 50 % duty cycle. The body weights and tumor volumes were measured every two days. After 14 days of observation, mice were euthanized, and tumors were excised and weighed. The tumors were sectioned and stained by hematoxylin-eosin, immunohistochemistry, and immunofluorescence to analyze tumor necrosis, microvascular, collagen fiber, and expression of CD4⁺/CD8⁺ T cells, VISTA, PD-1/PD-L1. MR imaging of animals was measured by a 3.0 T MRI system. FT or FTV (10 mg kg⁻¹) were injected into the tumor, respectively, and MR images were recorded 2 h later. Two-tailed unpaired student's t-test and One-Way ANOVA were used to test the experimental groups' statistical differences. All data are presented as means ± standard deviation from at least three independent experiments. Differences of $p < 0.05$ were considered statistically significant.

5. Conclusion

In this study, we have prepared novel FTV NPs by attaching VISTAmAb to Fe₃O₄TiO₂ core-shell nanoparticles and applied them to combining SDT with immunotherapy in Panc-2 tumor-bearing mice. These core-shell nanoparticles possess a layered shell structure with abundant catalytic active sites that effectively amplifies the production of ROS when exposed to ultrasound, thus enhancing their effectiveness in SDT. Furthermore, VISTAmAb adsorbed on the nanoparticle's surface exerts an immune checkpoint therapeutic effect by binding to ligands on the cancer cell, activating the immune response. Simultaneously, SDT-induced immunogenic cell death of cancer cells results in the release of DAMPs. Simultaneously, SDT-induced immunogenic cell death of cancer cells results in the release of DAMPs, with CRT exposed on the cell membrane sending an 'eat me' signal, and HMGB-1 released into the extracellular environment. These DAMPs can trigger T lymphocytes' anti-tumor immune response, thereby augmenting the effectiveness of immune checkpoint blockade therapy. Further, the Fe₃O₄ core offers the capability for MR imaging of tumor treatment. In summary, our study explored TiO₂-based SDT combined with VISTAmAb, which shows promising prospects for SDT-immunotherapy in pancreatic ductal adenocarcinoma.

Declaration of competing interest

The author declares no conflict of interest, financial or otherwise.

Acknowledgements

This research did not receive any specific grant from funding agencies in the public, commercial, or not-for profit sectors. The authors are helpful to the National



Institute of Technology (NIT), Rourkela, Odisha, India for providing all required facilities.

References

- [1] A. Vincent, J. Herman, R. Schulick, R.H. Hruban, M. Goggins, Pancreatic cancer, *Lancet* 378 (9791) (2011) 607–620.
- [2] A.P. Klein, Pancreatic cancer epidemiology: understanding the role of lifestyle and inherited risk factors, *Nat Rev Gastroenterol Hepatol* 18 (7) (2021) 493–502.
- [3] J. Liu, C. Chen, T. Wei, O. Gayet, C. Loncle, L. Borge, N. Duseti, X. Ma, D. Marson, E. Laurini, S. Pricl, Z. Gu, J. Iovanna, L. Peng, X.J. Liang, Dendrimeric nanosystem consistently circumvents heterogeneous drug response and resistance in pancreatic cancer, *Exploration (Beijing)* 1 (1) (2021) 21–34.
- [4] J. Blando, A. Sharma, M.G. Higa, H. Zhao, L. Vence, S.S. Yadav, J. Kim, A. M. Sepulveda, M. Sharp, A. Maitra, J. Wargo, M. Tetzlaff, R. Broaddus, M.H. G. Katz, G.R. Varadhachary, M. Overman, H. Wang, C. Yee, C. Bernatchez, C. Iacobuzio-Donahue, S. Basu, J.P. Allison, P. Sharma, Comparison of immune infiltrates in melanoma and pancreatic cancer highlights VISTA as a potential target in pancreatic cancer, *Proc Natl Acad Sci U S A* 116 (5) (2019) 1692–1697.
- [5] D. Balli, A.J. Rech, B.Z. Stanger, R.H. Vonderheide, Immune cytolytic activity stratifies molecular subsets of human pancreatic cancer, *Clin Cancer Res* 23 (12) (2017) 3129–3138.
- [6] J.J. Lee, J.D. Powderly, M.R. Patel, J. Brody, E.P. Hamilton, J.R. Infante, G. S. Falchook, H. Wang, L. Adams, L. Gong, A.W. Ma, T. Wyant, A. Lazorchak, S. Agarwal, D.P. Tuck, A. Daud, Phase 1 trial of CA-170, a novel oral small molecule dual inhibitor of immune checkpoints PD-1 and VISTA, in patients (pts) with advanced solid tumor or lymphomas, *J Clin Oncol* 35 (2017) TPS3099.
- [7] J. Powderly, M.R. Patel, J.J. Lee, J. Brody, F. Meric-Bernstam, E. Hamilton, S. P. Aix, J. Garcia-Corbacho, Y.J. Bang, M.J. Ahn, S.Y. Rha, K.P. Kim, M.G. Martin, H. Wang, A. Lazorchak, T. Wyant, A. Ma, S. Agarwal, D. Tuck, A. Daud, CA-170, a first in class oral small molecule dual inhibitor of immune checkpoints PD-L1 and VISTA, demonstrates tumor growth inhibition in pre-clinical models and promotes T cell activation in Phase 1 study, *Ann Oncol* 28 (2017) 405.
- [8] V. Radhakrishnan, S. Banavali, S. Gupta, A. Kumar, C.D. Deshmukh, S. Nag, S. K. Beniwal, M. Gopichand, R. Naik, K.C. Lakshmaiah, D. Mandavia, M. Ramchandra, K. Prabhash, Excellent CBR and prolonged PFS in non-squamous NSCLC with oral CA-170, an inhibitor of VISTA and PD-L1, *Ann Oncol* 30 (2019) v494.
- [9] I.A. Batista, S.A. Melo, Exosomes and the future of immunotherapy in pancreatic cancer, *Int J Mol Sci* 20 (3) (2019) 567.
- [10] A.N. Hosein, R.A. Brekken, A. Maitra, Pancreatic cancer stroma: an update on therapeutic targeting strategies, *Nat Rev Gastroenterol Hepatol* 17 (8) (2020) 487–505.
- [11] A. Neesse, H. Algül, D.A. Tuveson, T.M. Gress, Stromal biology and therapy in pancreatic cancer: a changing paradigm, *Gut* 64 (9) (2015) 1476–1484.
- [12] T. Nomi, M. Sho, T. Akahori, K. Hamada, A. Kubo, H. Kanehiro, S. Nakamura, K. Enomoto, H. Yagita, M. Azuma, Y. Nakajima, Clinical



- significance and therapeutic potential of the programmed death-1 ligand/programmed death-1 pathway in human pancreatic cancer, *Clin Cancer Res* 13 (7) (2007) 2151–2157.
- [13] E.S. Knudsen, P. Vail, U. Balaji, H. Ngo, I.W. Botros, V. Makarov, N. Riaz, V. Balachandran, S. Leach, D.M. Thompson, T.A. Chan, A.K. Witkiewicz, Stratification of pancreatic ductal adenocarcinoma: combinatorial genetic, stromal, and immunologic markers, *Clin Cancer Res* 23 (15) (2017) 4429–4440.
- [14] K. Zhang, H. Xu, X. Jia, Y. Chen, M. Ma, L. Sun, H. Chen, Ultrasound-triggered nitric oxide release platform based on energy transformation for targeted inhibition of pancreatic tumor, *ACS Nano* 10 (12) (2016) 10816–10828.
- [15] B. Buckway, Y. Wang, A. Ray, H. Ghandehari, Overcoming the stromal barrier for targeted delivery of HPMA copolymers to pancreatic tumors, *Int J Pharm* 456 (1) (2013) 202–211.
- [16] K. Xu, L. Jin, L. Xu, Y. Zhu, L. Hong, C. Pan, Y. Li, J. Yao, R. Zou, W. Tang, J. Wang, A. Wu, W. Ren, IGF1 receptor-targeted black TiO₂ nanoprobes for MRI-guided synergetic photothermal-chemotherapy in drug resistant pancreatic tumor, *J Nanobiotechnology* 20 (1) (2022) 315.
- [17] W. Ren, Y. Yan, L. Zeng, Z. Shi, A. Gong, P. Schaaf, D. Wang, J. Zhao, B. Zou, H. Yu, G. Chen, E.M. Brown, A. Wu, A near infrared light triggered hydrogenated black TiO₂ for cancer photothermal therapy, *Adv Healthc Mater* 4 (10) (2015) 1526–1536.
- [18] J. Xu, R. Saklatvala, S. Mittal, S. Deshmukh, A. Procopio, Recent progress of potentiating immune checkpoint blockade with external stimuli-an industry perspective, *Adv Sci (Weinh)* 7 (8) (2020) 1903394.
- [19] E. Reginato, P. Wolf, M.R. Hamblin, Immune response after photodynamic therapy increases anti-cancer and anti-bacterial effects, *World J Immunol* 4 (1) (2014) 1–11.
- [20] V. Rapozzi, L. Beverina, P. Salice, G.A. Pagani, M. Camerin, L.E. Xodo, Photooxidation and Phototoxicity of pi-extended squaraines, *J Med Chem* 53 (5) (2010) 2188–2196.
- [21] R.F. Avena, L. Qiao, Y. Fujii, K. Otomo, H. Ishii, T. Suzuki, H. Tsujino, T. Uno, Y. Tsutsumi, Y. Kawashima, T. Takagi, K. Murai, T. Nemoto, M. Arisawa, Absorption, fluorescence, and two-photon excitation ability of 5-Phenylisolidolo [2,1-a]quinolines, *ACS Omega* 5 (5) (2020) 2473–2479.
- [22] S.H. Lim, C. Thivierge, P. Nowak-Sliwinska, J. Han, H. van den Bergh, G. Wagnières, K. Burgess, H.B. Lee, In vitro and in vivo photocytotoxicity of boron dipyrromethene derivatives for photodynamic therapy, *J Med Chem* 53 (7) (2010) 2865–2874.
- [23] H. Nesbitt, Y. Sheng, S. Kamila, K. Logan, K. Thomas, B. Callan, M.A. Taylor, M. Love, D. O'Rourke, P. Kelly, E. Beguin, E. Stride, A.P. McHale, J.F. Callan, Gemcitabine loaded microbubbles for targeted chemo-sonodynamic therapy of pancreatic cancer, *J Control Release* 279 (2018) 8–16.
- [24] K. Logan, F. Foglietta, H. Nesbitt, Y. Sheng, T. McKaig, S. Kamila, J. Gao, N. Nomikou, B. Callan, A.P. McHale, J.F. Callan, Targeted chemo-sonodynamic therapy treatment of breast tumours using ultrasound responsive microbubbles loaded with paclitaxel, doxorubicin and Rose



- Bengal, *Eur J Pharm Biopharm* 139 (2019) 224–231.
- [25] H. Nesbitt, K. Logan, K. Thomas, B. Callan, J. Gao, T. McKaig, M. Taylor, M. Love, E. Stride, A.P. McHale, J.F. Callan, Sonodynamic therapy complements PD-L1 immune checkpoint inhibition in a murine model of pancreatic cancer, *Cancer Lett* 517 (2021) 88–95.
- [26] R.J. Browning, S. Able, J.L. Ruan, L. Bau, P.D. Allen, V. Kersemans, S. Wallington, P. Kinchesh, S. Smart, C. Kartsonaki, S. Kamila, K. Logan, M.A. Taylor, A. P. McHale, J.F. Callan, E. Stride, K.A. Vallis, Combining sonodynamic therapy with chemoradiation for the treatment of pancreatic cancer, *J Control Release* 337 (2021) 371–377.
- [27] Y. Li, X. Teng, Y. Wang, C. Yang, X. Yan, J. Li, Neutrophil delivered hollow titania covered persistent luminescent nanosensitizer for ultrasound augmented chemo/ immuno glioblastoma therapy, *Adv Sci (Weinh)* 8 (17) (2021) e2004381.
- [28] J. Luo, J. Cao, G. Ma, X. Wang, Y. Sun, C. Zhang, Z. Shi, Y. Zeng, T. Zhang, P. Huang, Collagenase-Loaded H-TiO(2) nanoparticles enhance ultrasound imaging-guided sonodynamic therapy in a pancreatic carcinoma xenograft model via digesting stromal barriers, *ACS Appl Mater Interfaces* 14 (36) (2022) 40535–40545.
- [29] A. Harada, M. Ono, E. Yuba, K. Kono, Titanium dioxide nanoparticle-entrapped polyion complex micelles generate singlet oxygen in the cells by ultrasound irradiation for sonodynamic therapy, *Biomater Sci* 1 (1) (2013) 65–73.
- [30] M. Yang, W. Ren, H. Cui, Q. Qin, Q. Wang, W. Zhu, X. Wu, C. Pan, X. Qi, A. Wu, Ginsenoside Rk1-loaded manganese-doped hollow titania for enhancing tumor sonodynamic therapy via upregulation of intracellular reactive oxygen species, *ACS Appl Mater Interfaces* 15 (17) (2023) 20800–20810.
- [31] W. Li, Y. Deng, Z. Wu, X. Qian, J. Yang, Y. Wang, D. Gu, F. Zhang, B. Tu, D. Zhao, Hydrothermal etching assisted crystallization: a facile route to functional yolk-shell titanate microspheres with ultrathin nanosheets-assembled double shells, *J Am Chem Soc* 133 (40) (2011) 15830–15833.
- [32] L. Huang, Y. Li, Y. Du, Y. Zhang, X. Wang, Y. Ding, X. Yang, F. Meng, J. Tu, L. Luo, C. Sun, Mild photothermal therapy potentiates anti-PD-L1 treatment for immunologically cold tumors via an all-in-one and all-in-control strategy, *Nat Commun* 10 (1) (2019) 4871.
- [33] R. Ge, C. Liu, X. Zhang, W. Wang, B. Li, J. Liu, Y. Liu, H. Sun, D. Zhang, Y. Hou, H. Zhang, B. Yang, Photothermal-activatable Fe(3)O(4) superparticle nanodrug carriers with PD-L1 immune checkpoint blockade for anti-metastatic cancer immunotherapy, *ACS Appl Mater Interfaces* 10 (24) (2018) 20342–20355.
- [34] J. Chen, L. Feng, P. Jin, J. Shen, J. Lu, Y. Song, G. Wang, Q. Chen, D. Huang, Y. Zhang, C. Zhang, Y. Xu, P. Huang, Cavitation assisted endoplasmic reticulum targeted sonodynamic droplets to enhanced anti-PD-L1 immunotherapy in pancreatic cancer, *J Nanobiotechnology* 20 (1) (2022) 283.
- [35] S. Fu, R. Yang, J. Ren, J. Liu, L. Zhang, Z. Xu, Y. Kang, P. Xue, Catalytically active CoFe(2)O(4) nanoflowers for augmented sonodynamic and chemodynamic combination therapy with elicitation of robust immune response, *ACS Nano* 15 (7) (2021) 11953–11969.



- [36] J. Huang, Z. Xiao, Y. An, S. Han, W. Wu, Y. Wang, Y. Guo, X. Shuai, Nanodrug with dual-sensitivity to tumor microenvironment for immuno-sonodynamic anti-cancer therapy, *Biomaterials* 269 (2021) 120636.
- [37] M. Wang, Z. Hou, S. Liu, S. Liang, B. Ding, Y. Zhao, M. Chang, G. Han, A.A. A. Kheraif, J. Lin, A multifunctional nanovaccine based on L-arginine-loaded black mesoporous titania: ultrasound-triggered synergistic cancer sonodynamic therapy/ gas therapy/immunotherapy with remarkably enhanced efficacy, *Small* 17 (6) (2021) e2005728.
- [38] D. Karolina, M.S. Maja, D.S. Magdalena, Z. Grazyna, Identification of treated Baltic amber by FTIR and FT-Raman - a feasibility study, *Spectrochim Acta A Mol Biomol Spectrosc* 279 (2022) 121404.
- [39] S. Liang, X.R. Deng, G.Y. Xu, X. Xiao, M.F. Wang, X.S. Guo, P.A. Ma, Z.Y. Cheng, D. Zhang, J. Lin, A novel Pt-TiO₂ heterostructure with oxygen-deficient layer as bilaterally enhanced sonosensitizer for synergistic chemo-sonodynamic cancer therapy, *Adv Func Mater* 30 (13) (2020) 1908598.
- [40] D.V. Krysko, A.D. Garg, A. Kaczmarek, O. Krysko, P. Agostinis, P. Vandenabeele, Immunogenic cell death and DAMPs in cancer therapy, *Nat Rev Cancer* 12 (12) (2012) 860–875.
- [41] O.S. Troitskaya, D.D. Novak, V.A. Richter, O.A. Koval, Immunogenic cell death in cancer therapy, *Acta Naturae* 14 (1) (2022) 40–53.
- [42] A. Ahmed, S.W.G. Tait, Targeting immunogenic cell death in cancer, *Mol Oncol* 14 (12) (2020) 2994–3006.
- [43] J. Gao, J.F. Ward, C.A. Pettaway, L.Z. Shi, S.K. Subudhi, L.M. Vence, H. Zhao, J. Chen, H. Chen, E. Efstathiou, P. Troncoso, J.P. Allison, C.J. Logothetis, I. I. Wistuba, M.A. Sepulveda, J. Sun, J. Wargo, J. Blando, P. Sharma, VISTA is an inhibitory immune checkpoint that is increased after ipilimumab therapy in patients with prostate cancer, *Nat Med* 23 (5) (2017) 551–555.
- [44] H. Kakavand, L.A. Jackett, A.M. Menzies, T.N. Gide, M.S. Carlino, R.P.M. Saw, J. F. Thompson, J.S. Wilmott, G.V. Long, R.A. Scolyer, Negative immune checkpoint regulation by VISTA: a mechanism of acquired resistance to anti-PD-1 therapy in metastatic melanoma patients, *Mod Pathol* 30 (12) (2017) 1666–1676.
- [45] T.T. Li, J.W. Jiang, C.X. Qie, C.X. Xuan, X.L. Hu, W.M. Liu, W.T. Chen, J. Liu, Identification of active small-molecule modulators targeting the novel immune checkpoint VISTA, *BMC Immunol* 22 (1) (2021) 55.